Avoiding dendrite formation by confining lithium deposition underneath Li-Sn coatings

Grace Whang[1,#], Qizhang Yan[4,#], Da Li[2,6], Ziyang Wei[2], Danielle Butts[1], Phillipe Sautet[2,3], Jian Luo[4,5], Bruce Dunn[1,*]

1 Department of Materials Science and Engineering; 2 Department of Chemistry and Biochemistry; 3 Department of Chemical and Biomolecular Engineering, University of California, Los Angeles, California 90095, USA

4 Department of Nanoengineering; 5 Program of Materials Science and Engineering, University of California San Diego, La Jolla, California 92093, USA

6 Institute of Process Engineering, Chinese Academy of Sciences, Beijing 100190, P.R. China

# These authors contributed equally; * Corresponding author

Abstract

The use of interfacial layers to stabilize the lithium surface is a popular research direction for improving the morphology of deposited lithium and suppressing lithium dendrite formation. This work considers a different approach to controlling dendrite formation where lithium is plated underneath an interfacial coating. In the present research, a Li-Sn intermetallic was chosen as a model system due to its lithium-rich intermetallic phases and high Li diffusivity. These coatings also exhibit a significantly higher Li exchange current than bare Li thus leading to better charge transfer kinetics. The exchange current is instrumental in determining whether lithium deposition occurs above or below the Li-Sn coating. High-resolution transmission electron microscopy and cryogenic focused ion beam scanning electron microscopy were used to identify the features associated with Li deposition. Atomic scale simulations provide insight as to the adsorption energies determining the deposition of lithium below the Li-Sn coating.

Introduction

The Li metal anode is considered to be a critical component for next generation rechargeable batteries due to its high theoretical capacity (3860 mAh g^{-1}) and low reduction potential (-3.040 V vs. S.H.E.) However, the formation of Li dendrites during repeated plating/stripping is a challenge that remains to be fully addressed [1–3]. The problem of Li dendrites is further complicated by the presence of a heterogeneous passivation layer known as the solid electrolyte interface (SEI) [4]. Due to the inherently low reduction potential of Li, the SEI formed at the Li surface upon contact with electrolyte results in the immediate electrolyte decomposition and formation of both organic and inorganic decomposition products[4–6]. While the SEI passivates the Li surface from further side reactions under static conditions, it is unstable under electrochemical cycling [7–9]. The compositional heterogeneity of the SEI imparts non-uniform Li-ion fluxes in addition to local differences in mechanical properties which promote the formation of Li dendrites and subsequent fracture of the SEI [10,11]. At higher current densities (> 1 mA cm^{-2}), dendritic morphologies with high surface areas dominate and continue to form new SEI resulting in continuous loss of active Li. In addition, the breakage of fragile Li dendrites results in the loss of electrical contact and formation of dead Li, which can be directly translated to poor coulombic efficiency [1]. The formation of Li dendrites is a multi-faceted problem that has been addressed through a broad range of approaches over past decades. Strategies employed thus far include the use of electrolyte additives to form a more compact and compositionally uniform SEI [12,13], high surface area three-dimensional current collectors to reduce the effective current density and accommodate Li volume change [14,15], separator engineering to mechanically block Li dendrites [16], lithophilic Li cages/hosts [15,17,18], and artificial coatings to stabilize the interface [19–25].

In this paper, we describe a different approach towards controlling Li dendrite formation, namely plating lithium underneath a coating formed on Li. This dual purpose coating can stabilize the reactive Li interface during plating/stripping and also facilitate in the transport of Li to allow for Li plating at the Li/coating interface. Although recent work has demonstrated lithium plating beneath a micrometers-thick intermetallic coating [21] there remain open questions on the relationship between the microstructure of the coating and the mechanism which enables Li deposition underneath. The plating of Li underneath a stabilizing layer offers a refreshing perspective on reframing the question of how to best suppress dendrite formation. By confining Li deposition to take place under the coating layer, the growth of lithium dendrites at the anode surface is effectively eliminated. In order to investigate the mechanism of plating underneath coating layers, a Li-Sn system was chosen as a model coating system due to its known ability to form lithium-rich intermetallic compounds [Fig. 1(c)] which exhibit high Li diffusivity [26–29]. The use of Li-Sn based coatings and substrates has been shown to demonstrate good plating kinetics and cycling performance [28–30]. However, to the best of our knowledge, Li deposition underneath lithium-tin based coatings has not been reported. In this study, we utilized transmission electron microscopy (TEM) to elucidate the microstructure of the solution processed Li-Sn intermetallic coating on Li, and cryogenic focused ion beam scanning electron microscopy (cryo-FIB-SEM) to characterize the interface morphology under different plating current densities. Through a combination of experiments and theoretical modelling, we identify conditions whereby Li can nucleate either above or underneath the Li-Sn intermetallic coating and thus provide new insight on the mechanism for this lithium plating process.

Results & Analysis

Li-Sn Composite Coating Fabrication and Characterization

Li-Sn composite coatings were formed through a solution processing route using a 50 mM solution of $SnCl_2$ dissolved in THF (Supplementary Fig. S1). Due to the reducing power and chemical reactivity of Li, the direct immersion of Li foil in the $SnCl_2$ solution resulted in the immediate reduction of the chloride solution on the lithium surface, producing a dark grey coating with intimate contact to the bulk foil. The plan-view SEM image in Fig. 1(b) reveals the microstructure of the coating surface. The reaction between the bare Li and the $SnCl_2$ solution produced a uniform coating consisting of submicron particle-like features. Cryo-FIB SEM was utilized to characterize the cross-section of the layer to reduce the risk of ion beam damage. As shown in Fig. 1(d), the coating is dense and has a thickness of around 1 μm. EDS mapping (Supplementary Fig. S2) confirms the uniform distribution of both Sn and Cl throughout the bulk coating.

The structure and phases of the coating were characterized with XRD and HRTEM. The (2Θ) diffraction peaks at 32.6 degrees and 46.8 degrees in Fig. 2(b) suggest that the coating likely contains both crystalline Li_7Sn_3 ($P12_1/m1$, ICSD-104785) and $Li_{13}Sn_5$ ($P\bar{3}m1$, ICSD-104786) phases. The broad diffraction peak at 38 degrees indicates the combination of the two Li-rich intermetallic phases, Li_7Sn_3 and $Li_{13}Sn_5$. Additionally, the broadness and low intensity of the diffraction peaks indicate that the intermetallic species present in the coating layer were either nanocrystalline and/or there were amorphous regions within the coating. HRTEM was utilized to further understand the microstructural characteristics of the layer which showed the presence of percolating nanocrystalline phases embedded in an amorphous matrix [Figs. 3(a) and 3(c-d)]. The Fast Fourier Transform (FFT) pattern of the entire region in Fig. 3(b) showed the existence of

Li_7Sn_3 and $Li_{13}Sn_5$ phases. In Fig. 3(c), the magnified TEM micrograph showed grains with *d*-spacing measured to be 0.20 nm and 0.23 nm. These values correspond to orientations of Li_7Sn_3 (102) and Li_7Sn_3 (212)/$Li_{13}Sn_5$ (110), respectively. The crystalline regions contain intermetallic grains that are <10 nm in diameter in addition to amorphous regions between the grains. The direct observation of amorphous regions could help to explain the broad and low intensity peaks observed for other solution processed intermetallic coatings [21,30].

Chlorine in the composite coating

The chlorine in the layer is suspected to be LiCl. In previous reports [21,32,33] LiCl was reported to form as a reaction product in a two-step reaction between Li and the metal chloride (MCl_x) [21]:

$$Li + MCl_x \rightarrow M + xLiCl.$$

$$yLi + zM \rightarrow Li_yM_z$$

Around 5% chlorine was detected by EDX analysis to be present within the intermetallic layer [(Fig. 2(a)]. Thus, the chlorine species is a minor constituent of the coating layer. To complement the EDX results, XPS was used to provide chemical information regarding the nanometer region near the surface (<10 nm) [34] of the coating. Both Cl $2p_{1/2}$ and Cl $2p_{3/2}$ were detected based on signals at 200.04 eV and 198.39 eV, respectively. These energies lie within comparable binding energies reported for the chlorine species produced under similar solution processing routes [21,32,33]. The Cl 2p signals could still be observed with no peak shifts after 15 minutes of argon ion etching (Supplementary Fig. S3), indicating that the chlorine species does not change in or near the surface of the coating while the cross-sectional EDS mapping demonstrated a uniform distribution of Cl signals throughout the bulk of the coating (Supplementary Fig. S2).

The fact that crystalline LiCl was not detected in either XRD or FFT patterns is not surprising [Figs. 2(b) and 3(b)]. This result is consistent with previous reports for metal chloride solution-processed intermetallic coatings [21,32,33] which assume the formation of an amorphous/nanocrystalline LiCl phase but provide no further evidence. In our study, the microstructure of the coating layer was revealed to contain amorphous regions (Fig. 3). To further assess the most likely chlorine species in the layer, density functional theory (DFT) calculations were performed to determine the most stable surfaces for $Li_{13}Sn_5$ and Li_7Sn_3. In a second series of calculations, a comparison of reaction energies was made for different Cl configurations on the most stable surfaces, inside the bulk intermetallic phases, or as a separate LiCl phase (See Supplementary Info II). Table I shows the reaction energies of various Cl configurations for both intermetallic phases. The formation of a separate LiCl phase is energetically more favorable over the doping of Cl into the intermetallic structure for both $Li_{13}Sn_5$ and Li_7Sn_3. While the presence of LiCl is not expected to take part in lithium transport due to its low lithium diffusivity, it can be of benefit to a coating layer by imparting fast surface diffusivity at the electrolyte/electrode interface which has been reported for lithium halide salts [35].

Although the question of whether an amorphous LiCl phase forms is outside the scope of this paper, an interesting possibility is that the amorphous region is a Li-Sn-Cl glass. Regions of binary or multi-component systems with decreased liquidus temperature are known to have increased glass forming ability [36] and the binary system of LiCl-$SnCl_2$ displays a eutectic at 488 K [37,38]. Thus, there is the prospect that $SnCl_2$ from the solution and LiCl from the reaction product react to form an amorphous phase with a eutectic-like composition. It is interesting to note that binary and multicomponent metal chloride based glasses have been known for decades [39–41].

Lithium Plating Exchange Current

In order to study the kinetics of the lithium plating process in the Li-Sn composite coatings, the Butler-Volmer equation was used to determine the exchange current of the coating layer system. The exchange current is a reflection of the kinetics of the charge transfer process and the rate of the reaction occurring at the electrode/electrolyte interface [42]. While Tafel plots are commonly employed to determine the exchange currents using the high overpotential approximation, it has recently been reported that the Butler Volmer Equation fails to describe the kinetics of lithium plating and stripping at overpotentials above 50 mV [43]. Therefore, the linear, low overpotential regime of the Butler-Volmer equation (See Methods section) was used to extrapolate the exchange current from a galvanostatic linear polarization experiment [Fig. 4(a)]. The lithium plating exchange current of the Li-Sn coating was found to be twice that of the bare lithium control, indicating more favorable charge transfer plating kinetics in the Li-Sn layer over the bare lithium control. The exchange current is inversely proportional to the charge transfer resistance [42], which can also be seen in the impedance measurements [Figs. 4(c) and 4(d)]. The Nyquist plot of the data not only shows a lower charge transfer resistance for the Li-Sn coating, but also demonstrates the ability of the coating to stabilize the lithium surface throughout the repeated plating and stripping during the galvanostatic linear polarization tests. In contrast, the bare lithium control suffers from a continuous increase in charge transfer resistance throughout the galvanostatic linear polarization measurement. This can be attributed to an increased surface area from non-uniform lithium deposition/stripping and the accompanying formation of more SEI, resulting in increased resistance [25,44–46]. The higher exchange current in combination with the stabilizing effect of the Li-Sn coating is expected to be favorable in terms of plating and stripping by imparting faster

plating/stripping kinetics in addition to providing surface stabilization during electrochemical cycling.

The Role of Plating Current Density in Lithium-Tin Coatings

In order to study the effect of the plating current density in Li-Sn coatings, two test case current densities were chosen: 1) a low current density of 0.1 mA cm^{-2} that is below the exchange current densities of both Li-Sn coating and bare lithium systems and 2) a high current density of 2 mA cm^{-2} that is above the exchange current density and represents a current density commonly used in Li plating studies [21,47,48]. For a bare lithium anode (no Li-Sn coating), lower currents, and thus smaller overpotentials (driving force), result in a larger critical radius for nucleation as shown by Equation 1 [48]:

$$r_c = -\frac{2\gamma_{n/e}\Omega}{F\eta} \quad [1]$$

where r_c is the critical nucleus radius, $\gamma_{n/e}$ is the interfacial energy between the Li nucleus and the electrolyte, Ω is the molecular volume of Li , *F* is Faraday's constant, and η is the overpotential. As a result, at lower current densities, more favorable plating morphologies with larger deposited features are typically observed whereas at high current densities of 2 mA cm^{-2}, smaller features with higher surface area morphologies are more favorable to form (Supplementary Fig. S4). However, unlike bare lithium, where lithium ions in the electrolyte have no other option but to plate on the lithium surface, Li-Sn coatings not only offer the possibility for heterogeneous lithium nucleation on top of the coating surface but also the possibility to plate underneath the coating. For plating to occur underneath, the charge transfer kinetics at the interface must be favorable in

addition to the transport of lithium through the layer, which must be relatively fast to minimize polarization and resistance within the coating.

Figure 5(c) shows the electrochemical signature of lithium plating in Li-Sn coatings plated at the low and high test case current densities. For the high plating current sample, the initial kink observed is commonly attributed to the nucleation overpotential for the lithium plating and the subsequent steadier overpotential after the nucleation event is related to the continuous growth of the deposits [48,49]. However, in the potential profile for the low plating current, there was no visible nucleation overpotential. The lack of a nucleation kink was also observed in a bare lithium symmetric cell plated at 0.1 mA cm^{-2} thus indicating that at the lower current densities, the nucleation and growth overpotentials are similar (Supplementary Fig. S5). However, in the bare lithium plating profile, the growth overpotential exhibited fluctuations which are likely the result of lithium deposition changing the electrode surface. In contrast, the Li-Sn sample plated at the low current density of 0.1mA cm^{-2} [Fig. 5(c)] demonstrated a stable overpotential with less than 1 mV change throughout the entire 40 hours of plating. The stability of the overpotential profile can be an indicator of the unchanging surface of the electrode as a result of lithium deposition underneath and preservation of the Li-Sn coating surface exposed to the electrolyte. In contrast, when lithium deposition occurs on the top of the Li-Sn coating, slight fluctuations in the overpotential [Fig. 5(c)] are exhibited and attributed to the changing surface area [Fig. 5(b)] associated with the non-uniform Li deposition [50,51].

In terms of the physical appearance of the electrodes, even at a plating capacity as high as 4 mAh cm^{-2}, no lithium plating was observed on the surface of the lithium tin coating for the lower plating

current density (0.1 mA cm^{-2}). A capacity of 4 mAh cm^{-2} equates to roughly 20 μm of plated lithium assuming uniform deposition and should be identifiable even from visual inspection. In comparing the different current densities, the plated lithium for the higher plating current density sample [Fig. 5(b)], is confined to the upper surface, covering the dark grey/black Li-Sn coating completely, while the lower plating current density sample retained the lithium tin coating morphology [Fig. 5(a)]. The drastic visual differences between the two samples indicate that there exists a critical current at which the lithium deposition location can be tuned to favor either plating at the surface or underneath the Li-Sn coating. This critical current is likely influenced by the exchange current density, which reflects the ease of charge transfer at the interface in addition to the fast transport of lithium through the coating via the lithium-rich intermetallic phase (*vide infra*). While plan-view SEM images show the absence of lithium on the surface of the lower plating current density sample, the use of cross-sectional Cryo-FIB SEM is able to elucidate the presence of buried lithium underneath the interface.

Probing above and beneath the Li-Sn layer

Cryo-FIB SEM was used to probe the Li plating morphology while minimizing the artifacts from the ion milling process [30,52]. For the Cryo-FIB samples, a smaller plating capacity of 1 mAh cm^{-2} was chosen to minimize the Cryo-FIB milling time. One key question to address was whether plated lithium could be distinguished from the bulk underlying lithium foil using the FIB milling process. As a control, a high plating current density sample (2 mA cm^{-2}, 1 mAh cm^{-2}) where lithium plated on top of the Li-Sn coating was analyzed to: 1) determine whether the Li-Sn layer could be

easily distinguished and 2) compare the plated lithium to the bulk lithium foil underneath the Li-Sn layer. Fig. 6(b) shows that at the higher current density of 2 mA cm^{-2}, heterogeneous nucleation of Li on top of the coating is observed and lithium deposition occurs on the top of the Li-Sn layer. The nucleation of Li is driven by overpotential [53] whereby larger currents result in larger overpotentials. The Everhart-Thornley Detector (ETD) SEM image in Fig. 6(b) shows the plated lithium on top of the Li-Sn coating. The plated Li above the coating can be better distinguished from the Li-Sn coating using a Backscattered Electron Detector (BSED), which provides greater contrast due to the atomic number dependence of backscattered electrons (Supplementary Fig. S6). The large difference between the atomic numbers of Sn (z=50) and Li (z=3), allow us to easily distinguish lithium (both plated and bulk foil) from the Li-Sn coating. While the plated and underlying bulk foil are both lithium, the plated lithium contains signals from the SEI (Fluorine, Sulfur, Carbon) which represents a characteristic feature of plated lithium observed in this study [Figs. 6(c)-6(f)]. The thickness of Li for 1 mAh cm^{-2}, assuming uniform deposition, is expected to be around 4.8 μm. This agrees well with the measured cross-section thickness for plated Li (4.87 ± 0.21 μm) indicating relatively uniform and dense Li deposition [Fig. 6(b)]. While Li plating occurred on top of the Li-Sn layer at higher current densities, the deposited Li layer exhibited a dense morphology. This demonstrates the critical influence of the substrate in lithium plating, which has previously shown favorable plating morphologies for tin-based interfaces [30]. The dense morphology for Li deposited at the higher current density of 2 mA cm^{-2} can be attributed to the fast surface diffusion at the Li-Sn coating interfaces. In addition to the contribution of the intermetallic phase, the presence of the chloride species also plays an important role in the surface diffusion of lithium when considering plating above the Li-Sn coating. The presence of lithium halide salts has been reported to improve plating morphology, which can be correlated to an

enhanced surface diffusion from the halide due to a reduced barrier for Li diffusion at the electrode/electrolyte interface [54,55]. Therefore, in our study, the dense, uniform, and dendrite-free plating morphology is attributed to both the Li-Sn intermetallic compounds and the chloride component in the composite coating.

For the lower plating current density (0.1 mA cm^{-2}, 1 mAh cm^{-2}), where the applied current was lower than the exchange current density, the Li plating process is more complex than what has been observed previously [21]. To complement the plan-view SEM image in Fig. 5(a) which showed no indication of Li plating on the surface of the coating, Cryo-FIB SEM was used to probe Li deposition below the surface. By comparing the secondary electron image with the backscattered electron image [Figs. 7(a) and 7(b)], the plated Li region (outlined in green) could be distinguished by both its morphology and composition. The plated Li beneath the Li-Sn coating contained porosity that helped distinguish it from the bulk Li foil. The EDX spectral mapping indicated a lack of tin signals from the region where morphology is different from the bulk Li while the EDX line scan showed an immediate decrease for both the tin and chlorine signals in the plated Li region (Supplementary Fig. S7). Similar to the Li plated on top of the coating at the higher current density, the Li plated underneath the coating also contained oxygen and sulfur signals from the electrolyte (Supplementary Fig. S8). The plated Li region underneath the coating in Fig. 7(a) was found to be less than the theoretical thickness of 4.8 μm. However, other regions within the sample were found to have plated Li thicknesses greater than 4.8 μm (Supplementary Fig. S9) indicating that the deposition of Li underneath the Li-Sn is non-uniform.

Li Adsorption Energy

The observation of Li plating underneath a micron thick coating offers new insight towards design principles for an effective Li interfacial layer that can both stabilize the reactive Li surface and serve as a passageway for the plating and stripping of Li underneath the coating. The prior notion that an ideal layer had to be in the nanometer range to mitigate polarization and resistance with growing film thickness [56,57] may be incomplete. In our study, for Li deposition to occur underneath a micron-thick Li intermetallic coating, the transport kinetics across the layer is critical and must be facilitated by high Li diffusivity via percolated Li-rich intermetallic grains within the coating layer. Li diffusivity in Li-rich tin intermetallics is several orders of magnitude higher [26,27] than self-diffusion of Li. The greater Li diffusivity translates to faster kinetics through the layer and the possibility of Li nucleation underneath the coating. In addition, because the coating layers are formed at room temperature within seconds, defects are likely to exist within the coating and could serve as additional pathways for Li transport.

Apart from high Li diffusivity, one additional driving force for Li deposition underneath is the adsorption energy of Li at the electrolyte/coating interface. To study the relationship between adsorption energy and lithium plating beneath the coating, the adsorption energy of Li on a $Li_{13}Sn_5$ surface was studied. A 33-layer (3×3) $Li_{13}Sn_5$ (001) symmetric slab was built and the adsorption energy was defined by two different approaches: 1) a simpler treatment using the computational Li electrode, namely, the chemical Li electrode (CLE) and 2) a more complex but also realistic treatment, namely, surface charging (SC), that explicitly takes the potential into account (See Methods Section).

For CLE, only G[Li], i.e., $\mu[Li^+ + e^-]$ is considered to be potential dependent and the adsorption energy is defined as:

$$G_{ads}(U) = E[Li@Li_{13}Sn_5] - \mu[Li^+ + e^-](U) - E[Li_{13}Sn_5] \quad [2]$$

Where G_{ads} (U) is the adsorption energy dependent on the potential vs Li/Li^+ electode, $E[Li@Li_{13}Sn_5]$ and $E[Li_{13}Sn_5]$ are the electronic energy of the adsorbed $Li_{13}Sn_5$ (001) surface and the bare $Li_{13}Sn_5$ (001) surface, respectively. For SC, both $G[Li@Li_{13}Sn_5]$ and $G[Li_{13}Sn_5]$ are considered to be quadratic functions of potential versus Li/Li^+ electrode and the adsorption energy is defined as:

$$G_{ads}(U) = G[Li@Li_{13}Sn_5](U) - \mu[Li^+ + e^-](U) - G[Li_{13}Sn_5](U) \quad [3]$$

Fig 8(b) shows the trend in adsorption energy per adsorbed Li atom as a function of surface coverage. In this case, surface coverage is defined by the number of adsorbed atoms divided by the number of atoms in a filled monolayer on the surface [Fig. 8(a)]. Interestingly, at the experimental overpotential of -0.005 V [Fig. 5(c)], the adsorption energy per atom is positive (hence unfavorable versus bulk Li) and peaks at a surface coverage from 1 to 2 and a value of [+0.05,+0.08] eV/atom (depending on the method), while thicker Li layers (3 and above) give a value close to zero (+0.01-0.02 eV/atom). These calculations on adsorption energy help to explain the experimentally observed difference in Li deposition location at different deposition rates. When the Li is deposited at a low rate, low surface coverage (1-2 monolayers) dominates, demonstrating a non favorable positive adsorption energy [Fig. 8(b)]. This positive adsorption energy provides a driving force for Li to penetrate the Li-Sn coating since the Li bulk below the coating corresponds to an adsorption energy of 0.005 eV/atom (see Methods Section). However, once the current density exceeds a certain threshold, the system is brought to a surface coverage > 2 where coating at the surface is almost as stable as bulk Li and there exists another pathway for

the system to approach the 0.005 eV/atom thermodynamic limit. That is, to continue the deposition and form a new Li bulk phase above the coating. By plating above and covering the Li-Sn surface, the system's adsorption energy is lowered and avoids the recrossing of the adsorption energy peak in Fig. 8(b).

During the lithium plating process, because the diffusion of Li ions in the liquid electrolyte is higher than the diffusion through the solid phase (i.e. Li-Sn coating), the rate limiting step in the coating system is the diffusion of Li through the Li-Sn coating. Therefore, there exists a threshold current density which should be governed by the Li diffusivity in the intermetallic coating which transports Li through the coating. The positive adsorption energy of adsorbed Li on the Li-Sn surface can help drive Li through the layer but there exists an optimal window for which plating underneath can be favored. At lower plating current densities, the high Li diffusivity of the coating layer is able to sustain the rate at which Li arrives at the coating surface and maintains a surface coverage that does not exceed the peak in positive absorption energy seen in Fig. (8b). However, at larger plating current densities, the rate of Li arriving at the coating surface exceeds the peak and it becomes more energetically favorable to form a new bulk lithium phase on top of the coating rather than transporting lithium through the coating.

Conclusion

In this work, we investigate the mechanism of Li plating underneath Li-Sn coatings which can serve as a strategy to mitigate dendrite formation. Li-Sn coatings were fabricated directly on lithium foil using a solution-based approach. HRTEM revealed a unique microstructure consisting of both Li-rich intermetallic grains and amorphous chloride regions. The plating kinetics for the Li-Sn coating demonstrated an exchange current twice that of bare lithium indicating enhanced

charge transfer kinetics in combination with the ability to stabilize the surface during plating/stripping. We demonstrate that by tuning the plating current density, the lithium deposition location can be modified. At current densities of 100 μA cm^{-2}, lithium deposition can be observed underneath the coating. At higher current densities of 2 mA cm^{-2}, heterogeneous nucleation of Li on top of the coating becomes more kinetically favorable compared to the diffusion of Li through the coating layer. Based on the microstructure of the coating and adsorption energy of Li at the intermetallic surface, we present new insights that help to explain lithium deposition underneath micrometer-thick intermetallic composite coatings. The results shown here suggest a novel approach for Li dendrite suppression.

Materials and Methods

Protective Coating Fabrication

The lithium-tin coating layer was fabricated using a solution-processed route in a sub-ppm Argon-filled glove box(VAC). Anhydrous Tin (II) Chloride (98%, Alfa Aesar) was dissolved and stirred into tetrahydrofuran(Sigma) to form a 50 mM Tin Chloride solution. Lithium metal foil (Alfa Aesar, 99.9%) was polished and subsequently immersed into the Tin(II) chloride solution for ~6-7 seconds to form a conformal dark coating on top of lithium. The coating was left to dry under ambient glovebox conditions for 3 hours and rinsed in dioxolane. For coin cell electrodes, lithium disks were punched out and pressed onto stainless steel spacers before immersing into the tin (II) chloride solution.

Coating Characterization

SEM (Nova NanoSEM230; Thermo Fisher Scientific) and EDX images (Noran System 7, Thermo Fisher Scientific) were obtained using an accelerating voltage of 10.0 kV to image the plan view morphology of the pristine and plated Li-Sn layers. The samples were exposed for a few seconds to ambient air during the sample transfer into the SEM chamber. EDX spectral maps were obtained to characterize the composition of the layer. X-ray photoelectron spectroscopy (XPS; Kratos Axis Ultra) with a monochromatic aluminum X-ray source was performed on the lithium tin coating layer using a voltage of 10kV and emission current of 10 mA. Peak calibration was performed using the adventitious carbon peak (284.8 eV). Analysis was carried out in CasaXPS software. TEM characterization of the coating layer was conducted using a JEOL 2800 TEM at 300 kV. The coating layer was gently scraped off from the Li metal surface and collected with a Cu grid inside an Ar-filled glovebox. The sample loading was conducted with direct Ar flow toward the sample holder to minimize air exposure. The coating cross-section was characterized using a FEI Scios Dualbeam FIB/SEM. A Ga-ion beam source at 30 kV was used to mill the sample. To preserve the coating and Li morphology, a cryo stage was used during the milling process. The cryo stage temperature was maintained below -180 °C using a heat exchanger in liquid nitrogen. X-ray Diffraction was performed using a PANalytical X'Pert Pro diffractometer using a Cu Kα (λ = 1.5418 Å) source. Samples were sealed in kapton to prevent air exposure. XRD patterns were recorded in the range of $30° < 2\theta < 70°$ using a 0.03° step size, a voltage of 45 kV, and a current of 40 mA.

Electrochemical Characterization

Galvanostatic plating/stripping experiments were conducted in a symmetric coin cell using a 25μm thick polypropylene separator and 80 μL of 1M lithium bis(trifluoromethane)sulfonimide (LiTFSI)

in dioxolane/dimethoxyethane (DOL/DME) (1:1 vol). Current densities of 100 μA cm^{-2} to 2mA cm^{-2} were used for the plating studies. For the galvanostatic linear polarization experiments, symmetric coin cells were subject to 3 cycles of plating and stripping for a set of current densities ranging from 5 to 50 μA cm^{-2}. In the calculation of the exchange current density, the plating and stripping overpotentials were assumed to be similar thus the plating overpotential was assumed to be half of the total overpotential and used to calculate the exchange current density. The low overpotential, linearized form of the Butler-Volmer equation was used in our study

$$i = i_o \left[exp\left(\frac{\alpha z F}{RT}\eta\right) - exp\left(\frac{(1-\alpha) z F}{RT}\eta\right)\right]$$

Assuming

$\alpha = 0.5$.

Using a linear approximation

$$e^x \approx 1 + x,$$

We obtain

$$i \approx i_o \frac{zF\eta}{RT}$$

Where $\eta = \frac{\eta_{total}}{2}$

where i is the current density, i_o is the exchange current density, α is the transfer coefficient, z is number of electrons involved in the reaction, F is Faraday's constant, η is the overpotential, R is the gas constant, and T is the temperature.

Computational Studies

The computations were carried out in the framework of density functional theory (DFT) [58] using the Vienna *ab initio* simulation package (VASP) [59,60]. The Perdew–Burke–Ernzerhof

generalized gradient approximation (PBE) [61] exchange–correlation functional is applied and the electron-ion interaction is described by the projector augmented-wave formalism (PAW) [62,63]. The plane wave cutoff energy was set as 500 eV. The convergence criteria of electronic structure and geometry optimization were set as 10^{-6} eV and 0.02 eV $Å^{-1}$, respectively. The reciprocal space was sampled on the gamma-centered meshes with a density around 0.15 $Å^{-1}$.

Solvation effect is described by linearized Poisson-Boltzmann equation using VaspSol addon package [64]. The dielectric constant is set as 7, corresponding to the experimental value of DOL. The cavity surface tension is set to 0 for numerical stability. This contribution is generally negligible for adsorption energies. The Debye screening length is set to give a 1M concentration of electrolyte.

In the molecular adsorption studies, the adsorption energy is defined as:

$$G_{ads} = G[Li@Li_{13}Sn_5] - G[Li] - G[Li_{13}Sn_5] \quad [4]$$

Where $G[Li@Li_{13}Sn_5]$, $G[Li]$ and $G[Li_{13}Sn_5]$ represent gibbs free energy of adsorbed $Li_{13}Sn_5$ (001) surface, adsorbates, and bare $Li_{13}Sn_5$ (001) surface, respectively. In the CLE approach, which is similar to the computational hydrogen electrode [65], in the right hand side, only G[Li], i.e., $\mu [Li^+ + e^-]$ is considered to be potential dependent. $\mu [Li^+ + e^-]$ in an electrochemical process is defined as:

$$\mu [Li^+ + e^-] (U) = E[Li, bulk] - eU[Li/Li^+] - k_b TpLi \quad [5]$$

Where E[Li, bulk] is the electronic energy of Li bulk, U[Li/Li^+] is potential vs Li/Li^+ electode, k_b is the boltzmann constant, T is the temperature, pLi is the concentration of Li. Explicitly writing all potential dependent terms gives:

$$G_{ads}(U) = E[Li@Li_{13}Sn_5] - \mu[Li^+ + e^-](U) - E[Li_{13}Sn_5] \quad [6]$$

Where G_{ads} (U) is the adsorption energy dependent on the potential vs Li/Li^+ electode, E[Li@$Li_{13}Sn_5$] and E[$Li_{13}Sn_5$] are the electronic energy of adsorbed $Li_{13}Sn_5$ (001) surface and bare $Li_{13}Sn_5$ (001) surface, respevtively. The pLi term in μ [Li^++e^-] (U) vanishes as the experimental Li electrolyte concentration is 1M. For a process where the Li forms extra layers at the other side of the coating, the E[Li@$Li_{13}Sn_5$], E[$Li_{13}Sn_5$], and E[Li, bulk] terms cancel out:

$$G_{ads}(U) = -eU \quad [7]$$

At the experimental condition, this gives 0.005 eV/atom adsorption energy.

In the SC approach [66,67], both G[Li@$Li_{13}Sn_5$] and G[$Li_{13}Sn_5$] are considered to be quadratic functions of potential versus Li/Li^+ electrode. Explicitly writing all potential dependent terms gives:

$$G_{ads}(U) = G[Li@Li_{13}Sn_5](U) - \mu[Li^+ + e^-](U) - G[Li_{13}Sn_5](U) \quad [8]$$

Where G[Li@$Li_{13}Sn_5$](U) and G[$Li_{13}Sn_5$](U) represent the gibbs free energy dependent on the potential vs Li/Li^+ electode of adsorbed $Li_{13}Sn_5$ (001) surface and bare $Li_{13}Sn_5$ (001) surface, respectively.

Acknowledgements

G.W. and Q.Y. contributed equally to this work. This work was supported as part of the Center for Synthetic Control Across Length-scales for Advancing Rechargeables (SCALAR), an Energy Frontier Research Center funded by the United States Department of Energy, Office of Science, Basic Energy Sciences under Award No. DESC0019381. D.L. is grateful for her one-year support from Joint PhD Training Fellowship Program from the University of Chinese Academy of Sciences. Lastly, the authors would like to thank Dr. Lele Peng for his helpful discussions throughout the progress of the project. This work used the shared user facilities at the San Diego Nanotechnology Infrastructure (SDNI) of UCSD, a member of the National Nanotechnology Coordinated Infrastructure supported by the National Science Foundation (Grant ECCS-1542148).

References

1. C. Fang, J. Li, M. Zhang, Y. Zhang, F. Yang, J. Z. Lee, M. H. Lee, J. Alvarado, M. A. Schroeder, Y. Yang, B. Lu, N. Williams, M. Ceja, L. Yang, M. Cai, J. Gu, K. Xu, X. Wang, and Y. S. Meng: Quantifying inactive lithium in lithium metal batteries. *Nature* **572**(7770), 511 (2019).
2. C. Fang, X. Wang, and Y. S. Meng: Key Issues Hindering a Practical Lithium-Metal Anode. *Trends Chem.* **0**(0), 1 (2019).
3. X. B. Cheng, R. Zhang, C. Z. Zhao, and Q. Zhang: Toward Safe Lithium Metal Anode in Rechargeable Batteries: A Review. *Chem. Rev.* **117**(15), 10403 (2017).
4. E. Peled: The Electrochemical Behavior of Alkali and Alkaline Earth Metals in Nonaqueous Battery Systems—The Solid Electrolyte Interphase Model. *J. Electrochem. Soc.* **126**(12), 2047 (1979).
5. J. Qian, W. A. Henderson, W. Xu, P. Bhattacharya, M. Engelhard, O. Borodin, and J. G. Zhang: High rate and stable cycling of lithium metal anode. *Nat. Commun.* **6** (2015).
6. J. B. Goodenough and Y. Kim: Challenges for rechargeable Li batteries. *Chem. Mater.* **22**(3), 587 (2010).
7. M. S. Whittingham: Electrical Energy Storage and Intercalation Chemistry. *Science (80-.).* **192**(4244), 1126 (1976).
8. B. D. Adams, J. Zheng, X. Ren, W. Xu, and J. G. Zhang: Accurate Determination of Coulombic Efficiency for Lithium Metal Anodes and Lithium Metal Batteries. *Adv. Energy Mater.* **8**(7), 1 (2018).
9. D. Aurbach: Review of selected electrode-solution interactions which determine the performance of Li and Li ion batteries. *J. Power Sources* **89**(2), 206 (2000).
10. X. B. Cheng, R. Zhang, C. Z. Zhao, F. Wei, J. G. Zhang, and Q. Zhang: A review of solid electrolyte interphases on lithium metal anode. *Adv. Sci.* **3**(3), 1 (2015).
11. M. D. Tikekar, S. Choudhury, Z. Tu, and L. A. Archer: Design principles for electrolytes and interfaces for stable lithium-metal batteries. *Nat. Energy* **1**(9), 1 (2016).
12. X. Q. Zhang, X. B. Cheng, X. Chen, C. Yan, and Q. Zhang: Fluoroethylene Carbonate Additives to Render Uniform Li Deposits in Lithium Metal Batteries. *Adv. Funct. Mater.*

27(10), 1 (2017).

13. D. Aurbach, K. Gamolsky, B. Markovsky, Y. Gofer, M. Schmidt, and U. Heider: On the use of vinylene carbonate (VC) as an additive to electrolyte solutions for Li-ion batteries. *Electrochim. Acta* **47**(9), 1423 (2002).
14. C. P. Yang, Y. X. Yin, S. F. Zhang, N. W. Li, and Y. G. Guo: Accommodating lithium into 3D current collectors with a submicron skeleton towards long-life lithium metal anodes. *Nat. Commun.* **6**(May) (2015).
15. Q. Yun, Y. B. He, W. Lv, Y. Zhao, B. Li, F. Kang, and Q. H. Yang: Chemical Dealloying Derived 3D Porous Current Collector for Li Metal Anodes. *Adv. Mater.* **28**(32), 6932 (2016).
16. K. Liu, D. Zhuo, H. W. Lee, W. Liu, D. Lin, Y. Lu, and Y. Cui: Extending the Life of Lithium-Based Rechargeable Batteries by Reaction of Lithium Dendrites with a Novel Silica Nanoparticle Sandwiched Separator. *Adv. Mater.* **29**(4), 1 (2017).
17. G. Zheng, S. W. Lee, Z. Liang, H. W. Lee, K. Yan, H. Yao, H. Wang, W. Li, S. Chu, and Y. Cui: Interconnected hollow carbon nanospheres for stable lithium metal anodes. *Nat. Nanotechnol.* **9**(8), 618 (2014).
18. Y. Chen, Z. Wang, X. Li, X. Yao, C. Wang, Y. Li, W. Xue, D. Yu, S. Y. Kim, F. Yang, A. Kushima, G. Zhang, H. Huang, N. Wu, Y. W. Mai, J. B. Goodenough, and J. Li: Li metal deposition and stripping in a solid-state battery via Coble creep. *Nature* **578**(7794), 251 (2020).
19. G. A. Umeda, E. Menke, M. Richard, K. L. Stamm, F. Wudl, and B. Dunn: Protection of lithium metal surfaces using tetraethoxysilane. *J. Mater. Chem.* **21**(5), 1593 (2011).
20. D. Lin, Y. Liu, W. Chen, G. Zhou, K. Liu, B. Dunn, and Y. Cui: Conformal Lithium Fluoride Protection Layer on Three-Dimensional Lithium by Nonhazardous Gaseous Reagent Freon. *Nano Lett.* **17**(6), 3731 (2017).
21. X. Liang, Q. Pang, I. R. Kochetkov, M. S. Sempere, H. Huang, X. Sun, and L. F. Nazar: A facile surface chemistry route to a stabilized lithium metal anode. *Nat. Energy* **6**, 17119 (2017).
22. Q. Yan, G. Whang, Z. Wei, S. T. Ko, P. Sautet, S. H. Tolbert, B. S. Dunn, and J. Luo: *Appl. Phys. Lett.* **117**, (2020).
23. F. Guo, C. Wu, H. Chen, F. Zhong, X. Ai, H. Yang, and J. Qian: Dendrite-free lithium

deposition by coating a lithiophilic heterogeneous metal layer on lithium metal anode. *Energy Storage Mater.* **24**(April 2019), 635 (2020).

24. L. Luo and A. Manthiram: An Artificial Protective Coating toward Dendrite-Free Lithium-Metal Anodes for Lithium–Sulfur Batteries. *Energy Technol.* **8**(7), 1 (2020).
25. R. Pathak, K. Chen, A. Gurung, K. M. Reza, B. Bahrami, J. Pokharel, A. Baniya, W. He, F. Wu, Y. Zhou, K. Xu, and Q. (Quinn) Qiao: Fluorinated hybrid solid-electrolyte-interphase for dendrite-free lithium deposition. *Nat. Commun.* **11**(1), 1 (2020).
26. A. Anani and R. A. Huggins: Technical Notes Kinetic and Thermodynamic Parameters of Several Binary Lithium. *J. Electrochem. Soc.* **134**(12), 3098 (1987).
27. C. J. Wen and R. A. Huggins: Chemical diffusion in intermediate phases in the lithium-tin system. *J. Solid State Chem.* **35**(3), 376 (1980).
28. M. Wan, S. Kang, L. Wang, H. W. Lee, G. W. Zheng, Y. Cui, and Y. Sun: Mechanical rolling formation of interpenetrated lithium metal/lithium tin alloy foil for ultrahigh-rate battery anode. *Nat. Commun.* **11**(1), 1 (2020).
29. H. Xu, S. Li, C. Zhang, X. Chen, W. Liu, Y. Zheng, Y. Xie, Y. Huang, and J. Li: Roll-to-roll prelithiation of Sn foil anode suppresses gassing and enables stable full-cell cycling of lithium ion batteries. *Energy Environ. Sci.* **12**(10), 2991 (2019).
30. Z. Tu, S. Choudhury, M. J. Zachman, S. Wei, K. Zhang, L. F. Kourkoutis, and L. A. Archer: Fast ion transport at solid-solid interfaces in hybrid battery anodes. *Nat. Energy* **3**(4), 310 (2018).
31. Z. Du, Z. Jiang, and C. Guo: Thermodynamic optimizing of the Li-Sn system. *Int. J. Mater. Res.* **97**(1), 10 (2006).
32. L. Lin, F. Liang, K. Zhang, H. Mao, J. Yang, and Y. Qian: Lithium phosphide/lithium chloride coating on lithium for advanced lithium metal anode. *J. Mater. Chem. A* **6**(32), 15859 (2018).
33. K. Liao, S. Wu, X. Mu, Q. Lu, M. Han, P. He, Z. Shao, and H. Zhou: Developing a “Water-Defendable” and “Dendrite-Free” Lithium-Metal Anode Using a Simple and Promising GeCl4 Pretreatment Method. *Adv. Mater.* **30**(36), 1 (2018).
34. J. F. Moulder, W. F. Stickle, and P. E. Sobol: Handbook of X-Ray Photoelectron Spectroscopy : A Reference Book of Standard Spectra for Identification and Interpretation of XPS Data (Physical Electronics, Inc., Eden Prairie, Minn., 1995).

35. Y. Ozhabes, D. Gunceler, and T. A. Arias: Stability and surface diffusion at lithium-electrolyte interphases with connections to dendrite suppression. *arXiv:1504.05799* 1 (2015).
36. H. Rawson: Inorganic Glass-Forming Systems (Academic Press, London, 1967).
37. G. Rack: The binary system SnCl2-LiCl. *Centr. Min. Geol.* **326**–**8** (1914).
38. Phase Equilibria Diagrams Online Database (NIST Standard Reference Database 31). *Am. Ceram. Soc. Natl. Inst. Stand. Technol.* Figure Number 3090 (2020).
39. M. Shojiya, M. Takahashi, R. Kanno, Y. Kawamoto, and K. Kadono: Optical transitions of Er3+ ions in ZnCl2-based glass. *J. Appl. Phys.* **82**(12), 6259 (1997).
40. K. Annapurna, R. N. Dwivedi, P. Kundu, and S. Buddhudu: Fluorescence properties of Sm3+: ZnCl2-BaCl2-LiCl glass. *Mater. Res. Bull.* **38**(3), 429 (2003).
41. A. J. Easteal, E. J. Sare, C. T. Moynihan, and C. A. Angell: Glass-transition temperature, electrical conductance, viscosity, molar volume, refractive index, and proton magnetic resonance study of chlorozinc complexation in the system ZnCl2+LiCl+H2O. *J. Solution Chem.* **3**(11), 807 (1974).
42. A. J. Bard and L. R. Faulkner: Electrochemical Methods: Fundamental and Applications, 2nd Editio (John Wiley & Sons, New York, NY, 2001).
43. D. T. Boyle, X. Kong, A. Pei, P. E. Rudnicki, F. Shi, W. Huang, Z. Bao, J. Qin, and Y. Cui: Transient Voltammetry with Ultramicroelectrodes Reveals the Electron Transfer Kinetics of Lithium Metal Anodes. *ACS Energy Lett.* **5**(3), 701 (2020).
44. G. Bieker, M. Winter, and P. Bieker: Electrochemical in situ investigations of SEI and dendrite formation on the lithium metal anode. *Phys. Chem. Chem. Phys.* **17**(14), 8670 (2015).
45. I. S. Kang, Y.-S. Lee, and D.-W. Kim: Improved Cycling Stability of Lithium Electrodes in Rechargeable Lithium Batteries. *J. Electrochem. Soc.* **161**(1), A53 (2014).
46. C. Wei, H. Fei, Y. An, Y. Tao, J. Feng, and Y. Qian: Uniform Li deposition by regulating the initial nucleation barrier: Via a simple liquid-metal coating for a dendrite-free Li-metal anode. *J. Mater. Chem. A* **7**(32), 18861 (2019).
47. K. Park and J. B. Goodenough: Dendrite-Suppressed Lithium Plating from a Liquid Electrolyte via Wetting of Li3N. *Adv. Energy Mater.* **7**(19), 1 (2017).
48. H. Jung, B. Lee, M. Lengyel, R. Axelbaum, J. Yoo, Y. S. Kim, and Y. S. Jun: Nanoscale:

In situ detection of nucleation and growth of Li electrodeposition at various current densities. *J. Mater. Chem. A* **6**(11), 4629 (2018).

49. F. Sagane, K. I. Ikeda, K. Okita, H. Sano, H. Sakaebe, and Y. Iriyama: Effects of current densities on the lithium plating morphology at a lithium phosphorus oxynitride glass electrolyte/copper thin film interface. *J. Power Sources* **233**, 34 (2013).
50. K. I. Popov, S. S. Djokić, and B. N. Grgur: in *Fundam. Asp. Electrometall.* (Springer US, Boston, MA, 2002), pp. 29–100.
51. A. Maraschky and R. Akolkar: Mechanism Explaining the Onset Time of Dendritic Lithium Electrodeposition via Considerations of the Li + Transport within the Solid Electrolyte Interphase . *J. Electrochem. Soc.* **165**(14), D696 (2018).
52. J. Z. Lee, T. A. Wynn, M. A. Schroeder, J. Alvarado, X. Wang, K. Xu, and Y. S. Meng: Cryogenic Focused Ion Beam Characterization of Lithium Metal Anodes. *ACS Energy Lett.* **4**(2), 489 (2019).
53. D. R. Ely and R. E. García: Heterogeneous Nucleation and Growth of Lithium Electrodeposits on Negative Electrodes. *J. Electrochem. Soc.* **160**(4), A662 (2013).
54. Y. Lu, Z. Tu, and L. A. Archer: Stable lithium electrodeposition in liquid and nanoporous solid electrolytes. *Nat. Mater.* **13**(10), 961 (2014).
55. Q. Pang, X. Liang, I. R. Kochetkov, P. Hartmann, and L. F. Nazar: Stabilizing Lithium Plating by a Biphasic Surface Layer Formed In Situ. *Angew. Chemie - Int. Ed.* **57**(31), 9795 (2018).
56. A. C. Kozen, C. F. Lin, A. J. Pearse, M. A. Schroeder, X. Han, L. Hu, S. B. Lee, G. W. Rubloff, and M. Noked: Next-Generation Lithium Metal Anode Engineering via Atomic Layer Deposition. *ACS Nano* **9**(6), 5884 (2015).
57. E. Kazyak, K. N. Wood, and N. P. Dasgupta: Improved Cycle Life and Stability of Lithium Metal Anodes through Ultrathin Atomic Layer Deposition Surface Treatments. *Chem. Mater.* **27**(18), 6457 (2015).
58. W. Kohn and L. J. Sham: Self-Consistent Equations Including Exchange and Correlation Effects. *Phys. Rev.* **140**(4A), A1133 (1965).
59. G. Kresse and J. Hafner: Ab initio molecular dynamics for liquid metals. *Phys. Rev. B* **47**(1), 558 (1993).
60. G. Kresse and J. Furthmüller: Efficient iterative schemes for ab initio total-energy

calculations using a plane-wave basis set. *Phys. Rev. B* **54**(16), 11169 (1996).

61. J. P. Perdew, K. Burke, and M. Ernzerhof: Generalized Gradient Approximation Made Simple. *Phys. Rev. Lett.* **77**(18), 3865 (1996).
62. P. E. Blöchl: Projector augmented-wave method. *Phys. Rev. B* **50**(24), 17953 (1994).
63. G. Kresse and D. Joubert: From ultrasoft pseudopotentials to the projector augmented-wave method. *Phys. Rev. B* **59**(3), 1758 (1999).
64. K. Mathew, R. Sundararaman, K. Letchworth-Weaver, T. A. Arias, and R. G. Hennig: Implicit solvation model for density-functional study of nanocrystal surfaces and reaction pathways. *J. Chem. Phys.* **140**(8) (2014).
65. J. K. Nørskov, J. Rossmeisl, A. Logadottir, L. Lindqvist, J. R. Kitchin, T. Bligaard, and H. Jónsson: Origin of the overpotential for oxygen reduction at a fuel-cell cathode. *J. Phys. Chem. B* **108**(46), 17886 (2004).
66. J. S. Filhol and M. L. Doublet: An ab initio study of surface electrochemical disproportionation: The case of a water monolayer adsorbed on a Pd(1 1 1) surface. *Catal. Today* **202**(1), 87 (2013).
67. J. S. Filhol and M. L. Doublet: Conceptual surface electrochemistry and new redox descriptors. *J. Phys. Chem. C* **118**(33), 19023 (2014).

Table I. The reaction energies (eV) to form a Cl doped LiSn intermetallic structures (either in the bulk or at the surface) and a separate LiCl phase for Li-Sn coating layer, energies are normalized as per $SnCl_2$ chemical formula. Considered reactions are described in the Supplementary Info II Equation 4-8.

Systems	$Li_{13}Sn_5$ Phase			Li_7Sn_3 Phase	
	Cl doped bulk	Cl doped (001) surface	Separate LiCl	Cl doped bulk	Separate LiCl
Reaction Energy (eV)	-5.72	-5.74	-5.86	-5.08	-5.72

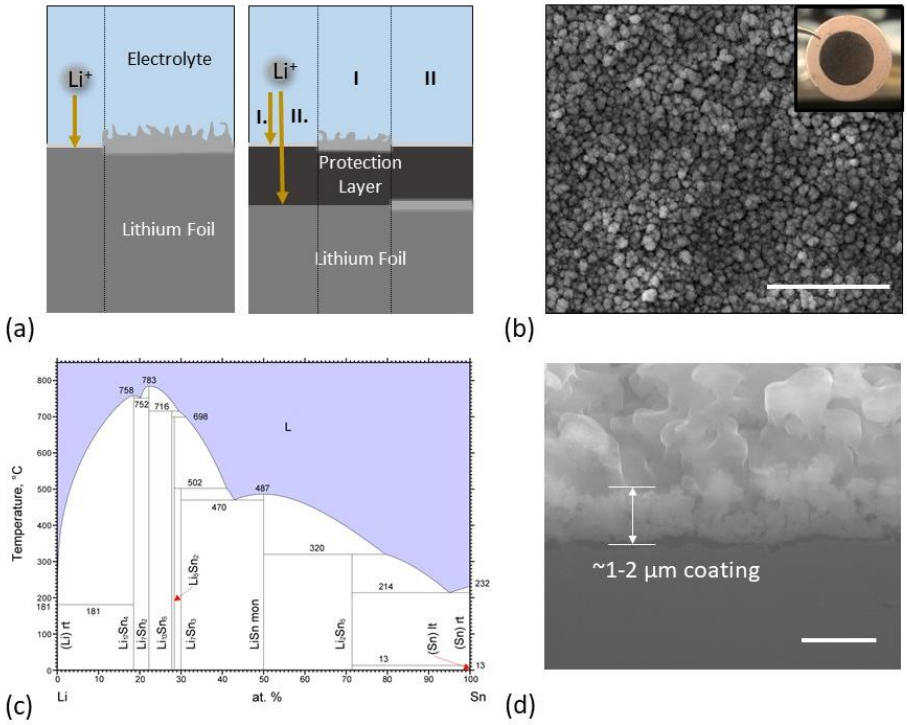

Figure 1: (a) Schematic comparing Li plating locations in bare lithium (left) and in a Li-Sn coating system (right) (b) Plan-view SEM image of coating morphology. Scale bar is 10 µm. Photograph of a pristine Li-Sn coating on a stainless steel spacer is shown on top right corner. (c) Lithium-Tin binary phase diagram [31] (d) cryo-FIB cross-sectional SEM image of Li-Sn coating on bulk Li foil. Scale bar is 1 µm.

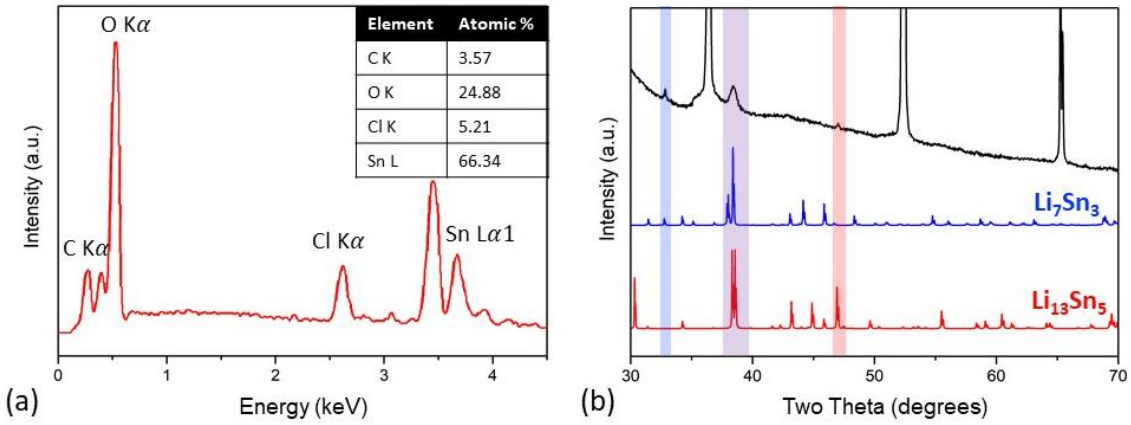

Figure 2: (a) Energy Dispersive Spectroscopy (EDS) of the Li-Sn coating showing both tin and chlorine signals and the corresponding atomic percentages. (b) X-ray Diffraction (XRD) pattern of Li-Sn coating (black) along with reference scans for Li_7Sn_3 (blue), and $Li_{13}Sn_5$ (red).

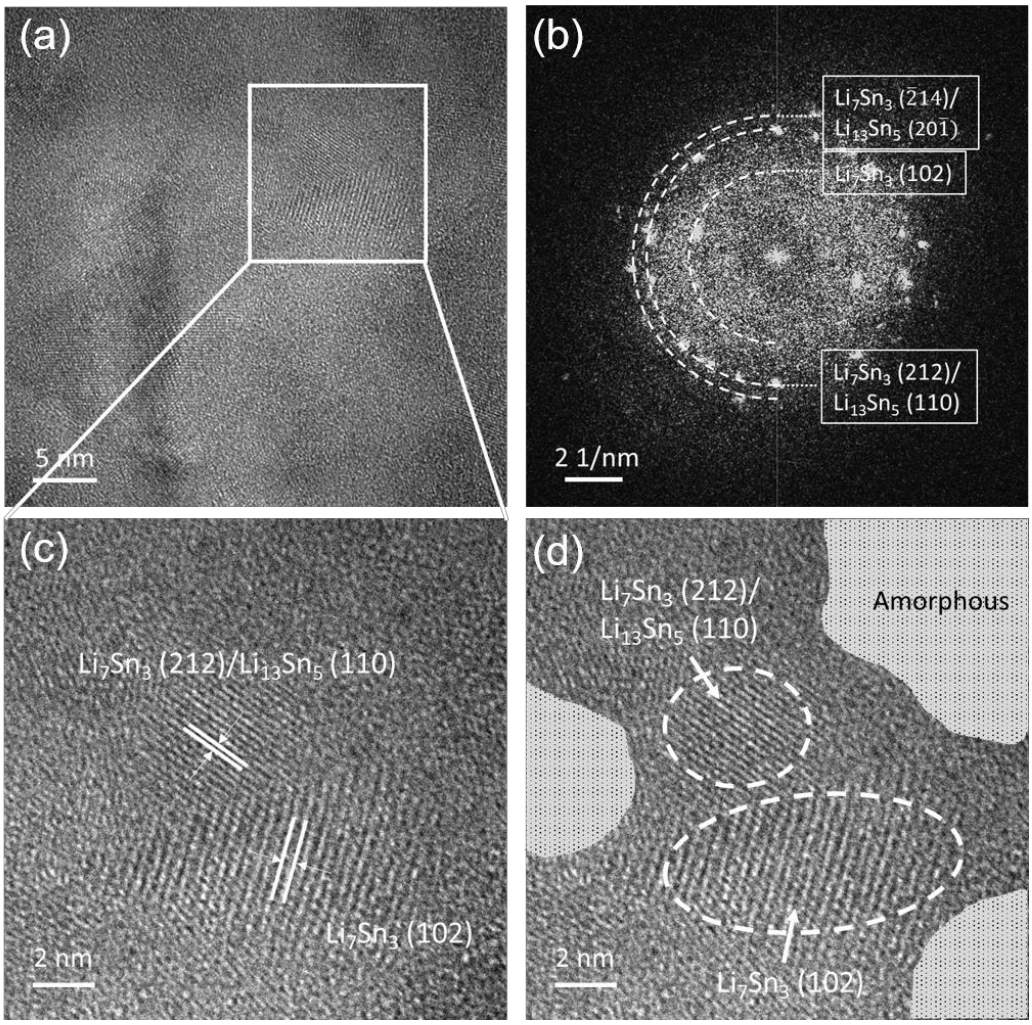

Figure 3: HRTEM micrographs of the Li-Sn composite coating. (a) Low-magnification image of composite coating. (b) FFT pattern of the entire region in figure 3a. (c) High-magnification image of the composite coating. (d) Phase distribution schematic overlaying the HRTEM image. The coating contains Li_7Sn_3, $Li_{13}Sn_5$, and amorphous regions.

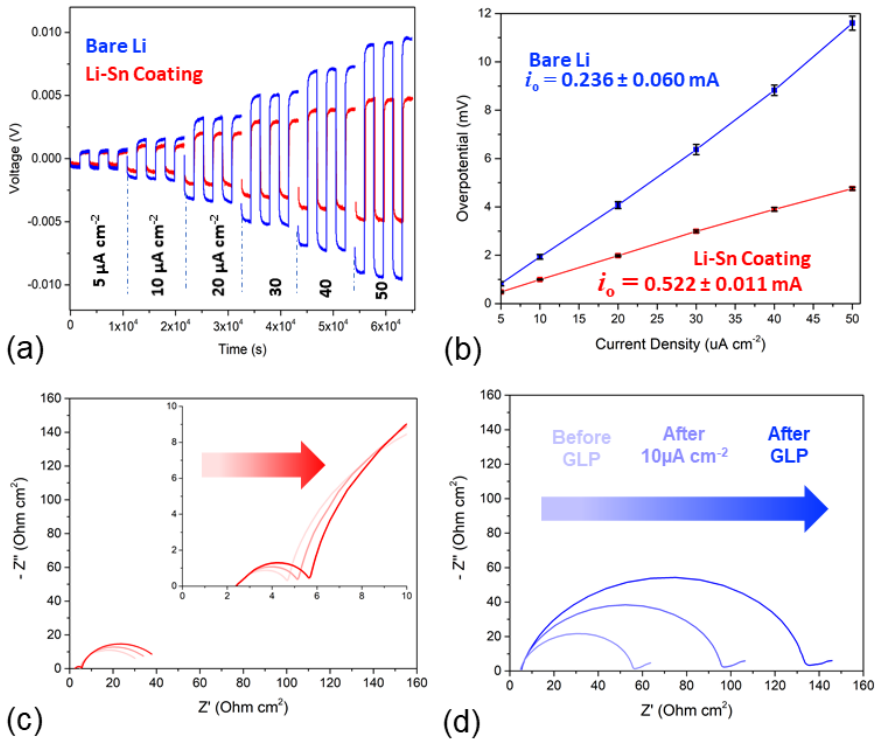

Figure 4: (a) Voltage vs. time profile of the galvanostatic linear polarization tests using current densities of 5, 10 , 20, 30, 40 and 50 µA cm^{-2} (b) Overpotential vs. current density plot demonstrating a linear trend for low overpotentials along with the corresponding exchange currents extrapolated from the galvanostatic linear polarization test. (c) Nyquist plot of the Li-Sn coated lithium symmetric cell. The light red trace represents the impedance before the test, the medium red trace represents the impedance during the test, and the dark red trace represents the impedance after the test. (d) Nyquist plot of a lithium control (no coating) symmetric cell which shows a larger initial impedance in addition to large increases throughout the test.

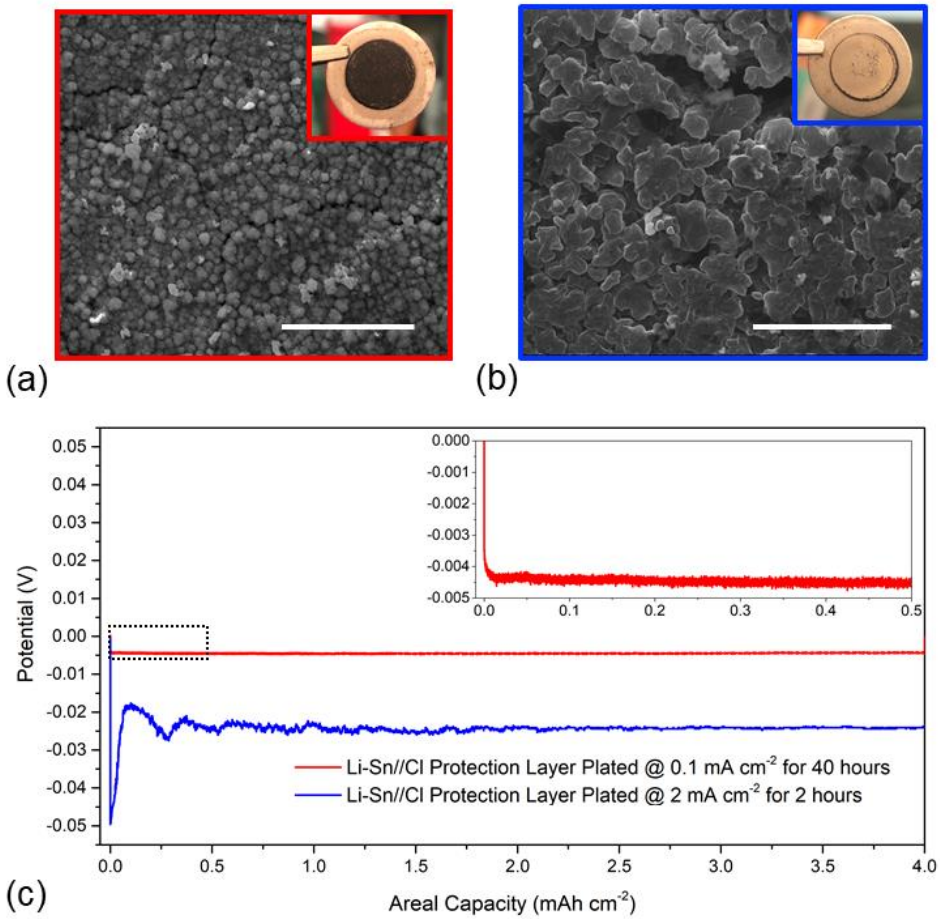

Figure 5: (a) Plan-view SEM of a Li-Sn coated lithium plated at 0.1 mA cm^{-2} for a plating capacity of 4 mAh cm^{-2}. Scale bar is 10 µm (b) Plan-view SEM of a Li-Sn coated lithium plated at 2 mA cm^{-2} for a plating capacity of 4 mAh cm^{-2}. Scale bar is Scale bar is 10 µm (c) Potential profile of Li-Sn coated Li plated at a current density of 0.1 mA cm^{-2} (red) and 2 mA cm^{-2} with the same areal capacity of 4 mAh cm^{-2}. Inset shows a zoom up of the 0.1 mA cm^{-2} plated sample which demonstrated a steady overpotential with less than 1 mV throughout the entire 40 hours.

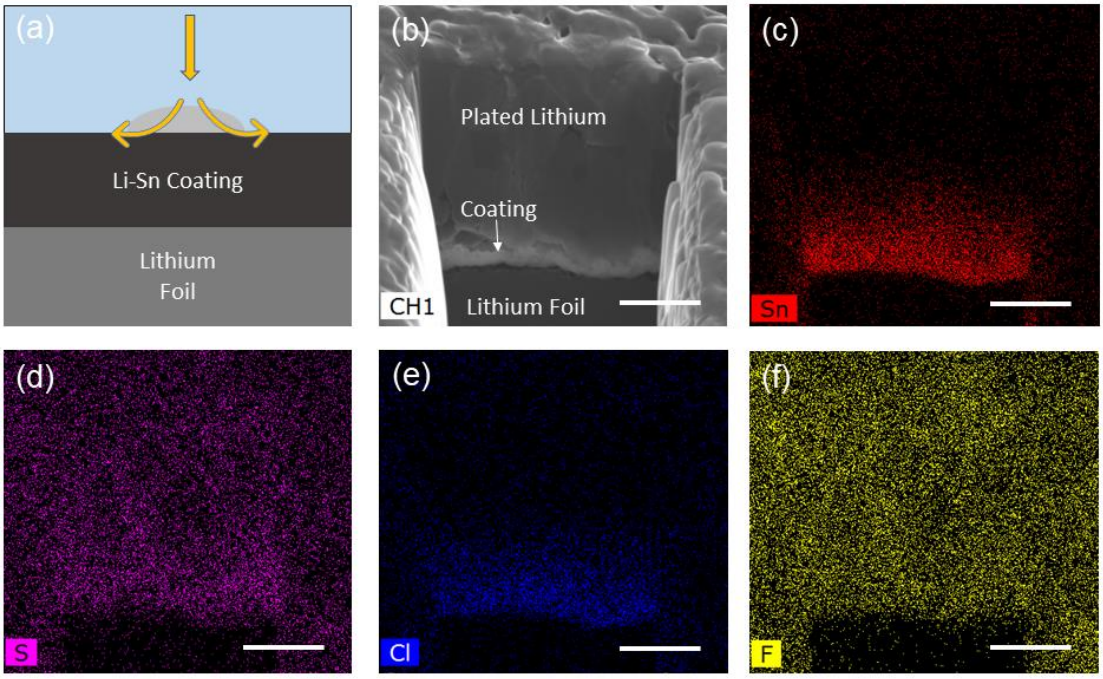

Figure 6: (a) graphic representing high plating current density case where lithium is observed to plate on top of the Li-Sn coating (b) Cryo FIB cross-section SEM of Li plated on top of Li-Sn coating at a current density of 2 mA cm^{-2} for a capacity of 1 mAh cm^{-2}. Scale bar is 2 µm. (c)-(f) EDX elemental mapping of the cross-section. Scale bar is 2 µm.

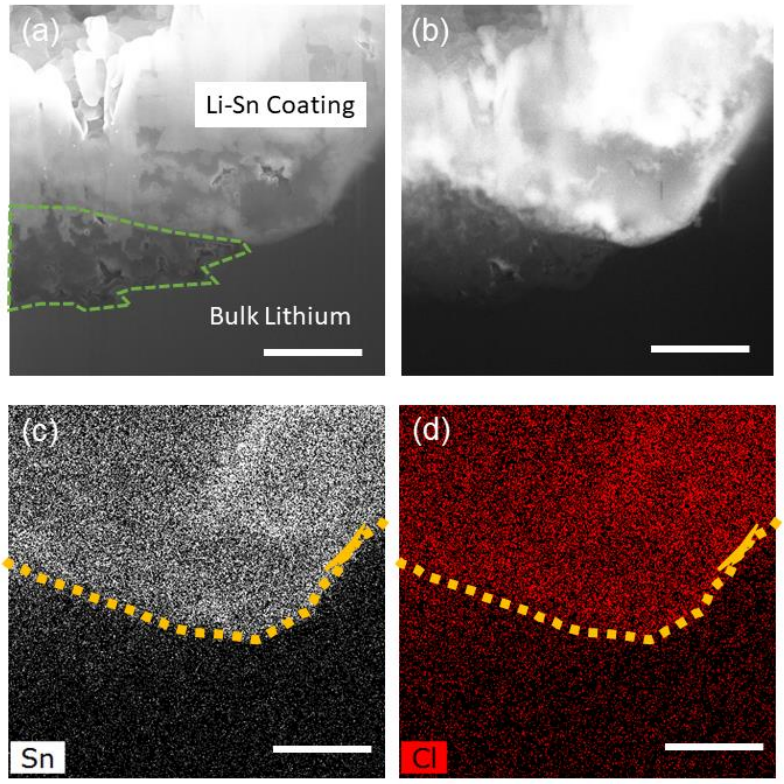

Figure 7: (a) Cryo FIB cross-section SEM of Li-Sn coating with lithium plated at a current density of 0.1 mA cm-2 for a capacity of 1 mAh cm-2. Plated lithium is outlined in green. Scale bar is 2 µm. (b) Backscattered Electron Detector (BSED) SEM image demonstrated a stark contrast between the plated lithium region and Li-Sn coating while showing similar electron signal between the bulk Li and plated Li. Scale bar is 2 µm. (c) EDX elemental mapping for tin. Scale bar is 2 µm. (d) EDX elemental mapping for chlorine. Scale bar is 2 µm.

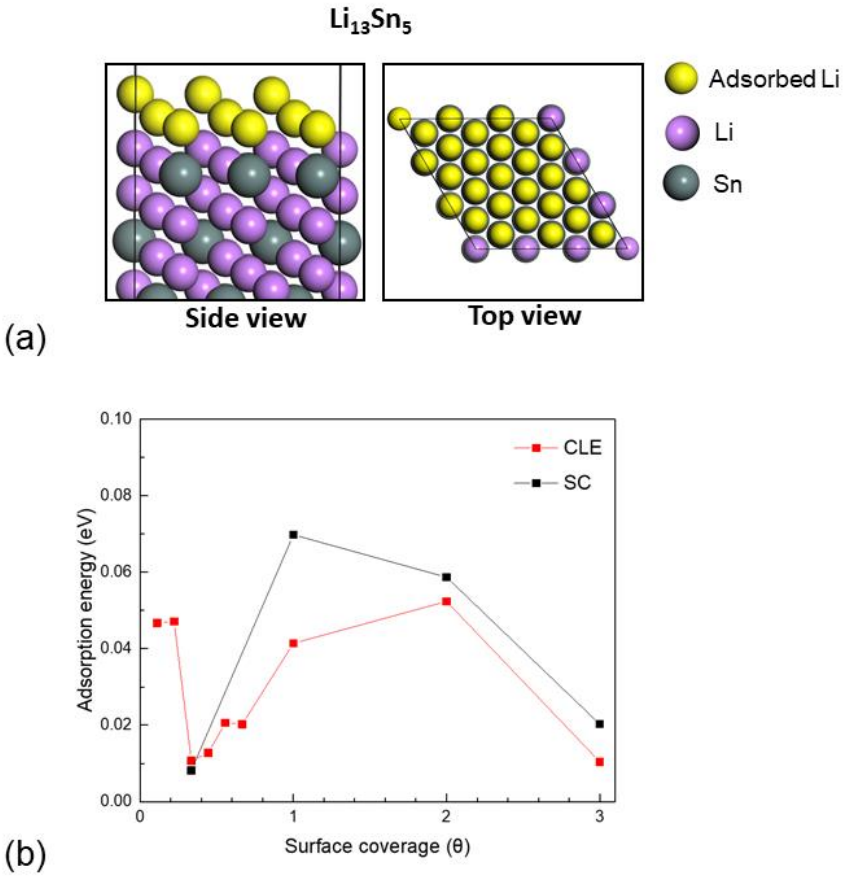

Figure 8. (a) Optimized geometries of adsorbed $Li_{13}Sn_5$ (001) surface with coverage as 3 and (b) variation of adsorption energy per adsorbed Li atom as a function of surface coverage.